magnetism

MDPI

*Article*

# Fast and Robust Capacitive Imaging of Cylindrical Non-Metallic Media

**Noshin Raisa, Yuki Gao, Mahindra Ganesh, Maryam Ravan and Reza K. Amineh ***

Department of Electrical and Computer Engineering, New York Institute of Technology, New York, NY 10023, USA; nraisa@nyit.edu (N.R.); ygao21@nyit.edu (Y.G.); mganes02@nyit.edu (M.G.); mravan@nyit.edu (M.R.)

* Correspondence: rkhalaja@nyit.edu

**Abstract:** In this paper, a unique approach to the imaging of non-metallic media using capacitive sensing is presented. By using customized sensor plates in single-ended and differential configurations, responses to hidden objects can be captured over a cylindrical aperture surrounding the inspected medium. Then, by processing the acquired data using a novel imaging technique based on the convolution theory, Fourier and inverse Fourier transforms, and exact low resolution electromagnetic tomography (eLORETA), images are reconstructed over multiple radial depths using the acquired sensor data. Imaging hidden objects over multiple depths has wide range of applications, from biomedical imaging to nondestructive testing of the materials. Performance of the proposed imaging technique is demonstrated via experimental results.

**Keywords:** electromagnetics; capacitive imaging; electromagnetic imaging; nondestructive evaluation; nondestructive testing



**Citation:** Raisa, N.; Gao, Y.; Ganesh, M.; Ravan, M.; Amineh, R.K. Fast and Robust Capacitive Imaging of Cylindrical Non-Metallic Media. *Magnetism* **2021**, *1*, 60–69. https://doi.org/10.3390/magnetism1010006

Academic Editor: Paolo Baccarelli

Received: 13 November 2021
Accepted: 1 December 2021
Published: 3 December 2021



## 1. Introduction

Along with many non-destructive evaluation (NDE) techniques such as ultrasound, eddy current, and X-ray, capacitive imaging (CI) is employed for material integrity inspections [1]. CI has been proven to be effective in biomedical applications [2,3], security screening [4], the inspection of reinforced concrete and dielectric surface characteristics of ceramic tiles [5], and in the NDE of glass fiber-reinforced polymer (GFPR) [6].

Typically, the CI technique uses electric fringing field from a pair of co-planar electrodes that can penetrate the non-conducting materials [7]. An AC voltage is applied to the electrodes, which causes a change in the electric field distribution while scanning the matter under inspection. The two plates of the sensor act as a capacitor and the change in the capacitance indicates variation in the internal dielectric properties of the material [8], internal defects [9], or surface flaws in non-metallic components [6]. One major advantage of the CI is that it is a non-contact technique [7].

Sensors can be constructed with electrodes that are made of conducting materials such as copper. Sensor fabrication can be implemented using microelectromechanical systems (MEMS), printed circuit board technology (PCB), or manually. In addition, CI sensors can be fabricated in various shapes and sizes for optimal usage. Among various design methods, sensor geometry is a major factor in determining the sensing performance to meet the requirements of the desired application [10]. Various geometries of CI sensors have been designed so far. For instance, a multi-segment cylindrical sensor was proposed in [11] to image continuous flow of liquids inside a pipeline. In [12], a helical wound electrode sensor and concave electrode sensor were developed for void fraction measurement. In [13], a coaxial cylindrical sensor was used to detect water levels. It is critical to know how sensors can be designed to optimize their performance for a specific application.

Here, we focus on the use of coplanar electrodes for capacitive sensing. The design parameters for a coplanar sensor include the number of electrodes and their arrangement,

as well as the electrodes' geometry, shielding, and guarding (e.g., see [14]). The geometry of the sensor includes the shape and size of the electrodes and the separation of the electrodes, which determines the performance of the sensor [10]. The shape of the electrodes can be circular, square [15], triangular [16], or more complex shapes such as a comb shape [17], which influences the sensor's performance in terms of its sensitivity and depth of penetration [18,19]. Shielding design for sensors is performed to eliminate stray capacitance or disturbance. Commonly, a shielding plate is held at ground potential and is used to achieve concise electric fields and to reduce electromagnetic interferences [19]. Electric fields and penetration depths with different electrode sizes and shapes have been discussed thoroughly in [19,20].

In this paper, we propose a non-contact and cost-effective CI approach to image objects in a cylindrical setup. To achieve resolution along the radial direction, we utilize single-ended and differential sensor configurations since these two sensor configurations allow for having two different ranges of sensing. The main novelty of the paper is in the use of a new image reconstruction approach, which is fast and efficient. The collected data over a cylindrical aperture are processed using convolution theory concept for a linear space-invariant system along with the Fourier and inverse Fourier transforms, and exact low resolution electromagnetic tomography (eLORETA) [21,22]. It is worth emphasizing that unlike in [21,22], in which eLORETA was employed for solving the systems of equations constructed in the spatial domain and for the application of electroencephalogram (EEG) brain imaging, here, eLORETA will be applied to many independent and small-dimensioned systems of equations constructed in the spatial frequency domain as explained in the Theory section. The performance of the proposed imaging technique will be demonstrated via experimental results.

## 2. Theory

In this section, we present the proposed imaging technique based on the data acquired by multiple capacitive sensors. Figure 1 illustrates the cylindrical capacitive imaging system in which $N_s$ capacitive sensors with various dimensions and configurations are employed to collect data over a cylindrical aperture with a radius of $r_A$ and a height of $z_A$.

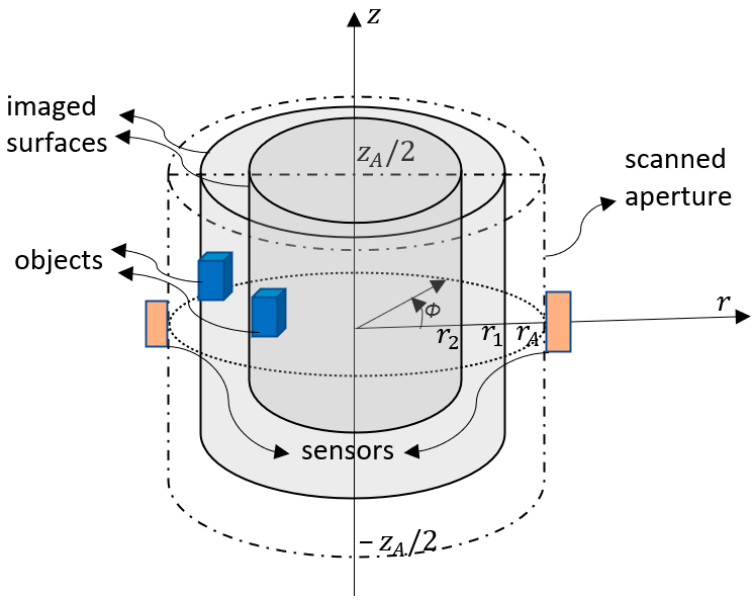


**Figure 1.** Illustration of the CI setup including different sensors placed at different azimuthal positions scanning a cylindrical aperture. The hidden objects are imaged over cylindrical surfaces with radii $r_j$ smaller than the radius of the scanned aperture $r_A$.

The number of smaples for each sensor along the azimuthal ($\phi$) and longitudinal ($z$) directions are denoted by $N_\phi$ and $N_z$, respectively. The objective is to reconstruct images over the cylindrical imaged surfaces at $r_j, j = 1, \ldots, N_r$.

We assume that the imaging system is linear and space-invariant. This allows us to employ the convolution theory. According to the convolution theory [23], in a linear space-invariant system, the response to an unknown input to the system can be written as the convolution of the impulse response (or point-spread function (PSF)) with that unknown input. Here, in our imaging system, the unknown inputs would be the shape functions of the objects, denoted by $f_j$, along the $z$ and $\phi$ directions at each cylindrical imaged surface $r = r_j$. In addition, by measuring the response due to a small object (here, referred to as the calibration object (CO)) representing an impulse function placed at cylindrical coordinate $(r_j, 0, 0)$, we obtain an approximation of the PSF of the system for the $j$-th imaged surface. The measured PSF by sensor $i$ ($i = 1, \ldots, N_s$) at azimuthal angles $\phi_k$ ($k = 1, \ldots, N_\phi$) and longitudinal positions $z_l$ (l = 1, ..., $N_z$) for the $j$-th imaged surface is denoted by $E^{CO}_{i,j}(\phi_k, z_l)$. The measured response for unknown objects over the $j$-th imaged surface can be then written as the convolution of the collected PSF $E^{CO}_{i,j}(\phi_k, z_l)$ with the shape function of the objects over that surface $f_j(\phi_k, z_l)$.

The goal of the imaging technique is to estimate the shape function of the objects under test (OUTs) $f_j(\phi_k, z_l)$ at each imaged surface at $r_j, j = 1, \ldots, N_r$. The total responses $E^O_i(\phi_k, z_l)$ with the presence of the OUTs on all the imaged surfaces are measured over the aperture. Using the convolution theory, these responses can be written as the sum of the convolutions of the PSF for each imaged surface at $r_j$, $E^{CO}_{i,j}(\phi_k, z_l)$, with the shape function of the OUTs for the corresponding surface $f_j(\phi_k, z_l)$ as [24]:

$$E^O_i(\phi_k, z_l) = \sum_{j=1}^{Nr} E^{CO}_{i,j}(\phi_k, z_l) *_\phi *_z f_j(\phi_k, z_l) \tag{1}$$

where $*_\phi$ and $*_z$ denote the convolutions along the $\phi$ and $z$ directions. Writing (1) for all the sensors $N_s$ and applying discrete-time Fourier transform (DTFT) and discrete Fourier transform (DFT) to both sides of the equations along $z$ and $\phi$ directions, respectively, leads to the following system of equations at each spatial frequency pair $\boldsymbol{\kappa} = (k_\phi, k_z)$ ($k_\phi$ and $k_z$ are Fourier variables corresponding to $\phi$ and $z$, respectively) [25,26]:

$$\underline{\underline{\widetilde{\mathbf{E}}}}^O_{(N_S \times 1)} = \underline{\underline{\widetilde{\mathbf{D}}}}_{(N_S \times N_r)} \underline{\underline{\widetilde{\mathbf{F}}}}_{(N_r \times 1)} \tag{2}$$

where

$$\underline{\underline{\widetilde{\mathbf{E}}}}^O_{(N_S \times 1)} = \underline{\underline{\mathrm{L}}} \begin{bmatrix} \widetilde{\widetilde{E}}^O_1(\boldsymbol{\kappa}) \\ \vdots \\ \widetilde{\widetilde{E}}^O_{N_S}(\boldsymbol{\kappa}) \end{bmatrix} \tag{3}$$

$$\underline{\underline{\widetilde{\mathbf{D}}}}_{(N_S \times N_r)} = \underline{\underline{\mathrm{L}}} \begin{bmatrix} \widetilde{\widetilde{E}}^{CO}_{1,1}(\boldsymbol{\kappa}) & \cdots & \widetilde{\widetilde{E}}^{CO}_{1,N_r}(\boldsymbol{\kappa}) \\ \vdots & \ddots & \vdots \\ \widetilde{\widetilde{E}}^{CO}_{N_S,1}(\boldsymbol{\kappa}) & \cdots & \widetilde{\widetilde{E}}^{CO}_{N_S,N_r}(\boldsymbol{\kappa}) \end{bmatrix} \tag{4}$$

and

$$\underline{\underline{\widetilde{\mathbf{F}}}} = \begin{bmatrix} \widetilde{\widetilde{f}}_1(\boldsymbol{\kappa}) \\ \vdots \\ \widetilde{\widetilde{f}}_{N_r}(\boldsymbol{\kappa}) \end{bmatrix} \tag{5}$$

where $\tilde{\tilde{E}}_i^O(\boldsymbol{\kappa})$, $\tilde{\tilde{E}}_{i,j}^{CO}(\boldsymbol{\kappa})$, and $\tilde{\tilde{f}}_j(\boldsymbol{\kappa})$ are obtained by taking DFT along $\phi$ and DTFT along $z$ of $E_i^O(\phi_k, z_l)$, $E_{i,j}^{CO}(\phi_k, z_l)$, and $f_j(\phi_k, z_l)$, respectively. The matrix $\underline{\underline{\mathrm{L}}}_{(N_S \times N_S)} = \underline{\underline{\mathrm{I}}} - \underline{1}\underline{1}^{\mathrm{T}}/\underline{1}^{\mathrm{T}}\underline{1}$ is the centering matrix that is the average reference operator, where $\underline{\underline{\mathrm{I}}}_{(N_S \times N_S)}$ is the identity matrix and $\underline{1}_{(N_S \times 1)}$ is a vector of ones. The $\underline{\underline{\mathrm{L}}}$ matrix is a symmetric and idempotent matrix. When it is multiplied with any vector, it has the effect of subtracting the mean of the components of the vector from every component of that vector.

At each $\boldsymbol{\kappa} = (k_\phi, k_z)$, the system of equations in (2) is solved to obtain $\tilde{\tilde{f}}_j(\boldsymbol{\kappa})$, $j = 1, \ldots, N_r$. Then, inverse DTFT along $z$ and inverse DFT along $\phi$ are applied to $\tilde{\tilde{f}}_j(\boldsymbol{\kappa})$ to obtain $f_j(\phi_k, z_l)$ which are considered as the reconstcruted images.

Here, we propose using the eLORETA approach to solve the systems of equations [21]. It is a genuine inverse solution with exact localization in the presence of measurement and structured noise. For this purpose, lets consider the problem of the general weighted minimum norm as [22]:

$$\min_{\underline{\tilde{\tilde{\mathbf{F}}}}} \left[ \| \underline{\tilde{\tilde{\mathbf{E}}}}^O - \underline{\underline{\tilde{\tilde{\mathbf{D}}}}}\, \underline{\tilde{\tilde{\mathbf{F}}}} \|^2 + \alpha \underline{\tilde{\tilde{\mathbf{F}}}}^{\mathrm{H}}\, \underline{\underline{\mathrm{W}}}\, \underline{\tilde{\tilde{\mathbf{F}}}} \right] \tag{6}$$

where $\underline{\underline{\mathrm{W}}}_{N_r \times N_r}$ is the symmetric weight matrix and $\alpha \geq 0$ is the regularization parameter. The estimated solution of (6) is linear and can be written as:

$$\hat{\underline{\tilde{\tilde{\mathbf{F}}}}} = \underline{\underline{\mathrm{Q}}}\, \underline{\tilde{\tilde{\mathbf{E}}}}^O \tag{7}$$

where

$$\underline{\underline{\mathrm{Q}}}_{(N_r \times N_S)} = \underline{\underline{\mathrm{W}}}^{-1}\, \underline{\underline{\tilde{\tilde{\mathbf{D}}}}}^{\mathrm{H}} \left[ \underline{\underline{\tilde{\tilde{\mathbf{D}}}}}\, \underline{\underline{\mathrm{W}}}^{-1} \underline{\underline{\tilde{\tilde{\mathbf{D}}}}}^{\mathrm{H}} + \alpha \underline{\underline{\mathrm{L}}} \right]^{+} \tag{8}$$

$\alpha \underline{\underline{\mathrm{L}}}$ is the covariance matrix of the noise, and $\underline{\underline{\mathrm{W}}}^{-1}_{N_r \times N_r}$ is the covariance matrix for $\underline{\tilde{\tilde{\mathbf{F}}}}$.

Then, we extend the linear equation in (2) to include additive measurement noise while we assume that $\underline{\tilde{\tilde{\mathbf{F}}}}$ and the measurement noise are independent. This allows us to write the covariance matrix for $\underline{\tilde{\tilde{\mathbf{E}}}}^O$ as:

$$\mathrm{cov}(\underline{\tilde{\tilde{\mathbf{E}}}}^O) = \underline{\underline{\tilde{\tilde{\mathbf{D}}}}}\, \underline{\underline{\mathrm{W}}}^{-1} \underline{\underline{\tilde{\tilde{\mathbf{D}}}}}^{\mathrm{H}} + \alpha \underline{\underline{\mathrm{L}}} \tag{9}$$

Using the linear relation between $\hat{\underline{\tilde{\tilde{\mathbf{F}}}}}$ and $\underline{\tilde{\tilde{\mathbf{E}}}}^O$ in (7), the covariance matrix for $\hat{\underline{\tilde{\tilde{\mathbf{F}}}}}$ can be then written as:

$$\mathrm{cov}(\hat{\underline{\tilde{\tilde{\mathbf{F}}}}}) = \underline{\underline{\mathrm{W}}}^{-1} \underline{\underline{\tilde{\tilde{\mathbf{D}}}}}^{\mathrm{H}} \left( \underline{\underline{\tilde{\tilde{\mathbf{D}}}}}\, \underline{\underline{\mathrm{W}}}^{-1} \underline{\underline{\tilde{\tilde{\mathbf{D}}}}}^{\mathrm{H}} + \alpha \underline{\underline{\mathrm{L}}} \right)^{+} \underline{\underline{\tilde{\tilde{\mathbf{D}}}}}\, \underline{\underline{\mathrm{W}}}^{-1} \tag{10}$$

When restricting $\underline{\underline{\mathrm{W}}}$ to a diagonal matrix, the solution to the following problem:

$$\min_{\underline{\underline{\mathrm{W}}}} \| \underline{\underline{\mathrm{I}}} - \mathrm{cov}(\hat{\underline{\tilde{\tilde{\mathbf{F}}}}}) \|^2 = \min_{\underline{\underline{\mathrm{W}}}} \| \underline{\underline{\mathrm{I}}} - \underline{\underline{\mathrm{W}}}^{-1} \underline{\underline{\tilde{\tilde{\mathbf{D}}}}}^{\mathrm{H}} \left( \underline{\underline{\tilde{\tilde{\mathbf{D}}}}}\, \underline{\underline{\mathrm{W}}}^{-1} \underline{\underline{\tilde{\tilde{\mathbf{D}}}}}^{\mathrm{H}} + \alpha \underline{\underline{\mathrm{L}}} \right)^{+} \underline{\underline{\tilde{\tilde{\mathbf{D}}}}}\, \underline{\underline{\mathrm{W}}}^{-1} \|^2 \tag{11}$$

provides an inverse solution (7) for which the localization error is zero. To find the diagonal weight $\underline{\underline{\mathrm{W}}}$ that solves the problem in (11), the following iterative approach is implemented [21,22]:

1. For a given $\underline{\underline{\tilde{\tilde{\mathbf{D}}}}}$ and regularization parameter $\alpha$, initialize $\underline{\underline{\mathrm{W}}}$ as the identity matrix.
2. Using the current diagonal matrix $\underline{\underline{\mathrm{W}}}$, find matrix $\underline{\underline{\mathbf{M}}}$ as:

$$\underline{\underline{\mathbf{M}}}_{(N_S \times N_S)} = \left( \underline{\underline{\tilde{\tilde{\mathbf{D}}}}}\, \underline{\underline{\mathrm{W}}}^{-1} \underline{\underline{\tilde{\tilde{\mathbf{D}}}}}^{\mathrm{H}} + \alpha \underline{\underline{\mathrm{L}}} \right)^{+} \tag{12}$$

3. For $i = 1$ to $N_r$, compute the updated diagonal matrix $\underline{\underline{W}}$ as:

$$\underline{\underline{W}}(i,i) = \sqrt{(\underline{\underline{\tilde{D}}}^{H} \underline{\underline{M}} \underline{\underline{\tilde{D}}})} \tag{13}$$

4. Compare the current $\underline{\underline{W}}$ with the one obtained from the previous iteration and, if the difference is larger than a predetermined threshold, then repeat steps 2 and 3 until convergence of $\underline{\underline{W}}$ is reached (negligible changes in $\underline{\underline{W}}$ between two consecutive iterations).

Finally, the estimated diagonal matrix $\underline{\underline{W}}$ obtained from the above iterative method is employed to compute the matrix $\underline{\underline{Q}}$ in (8). This, in turn, provides the estimated solution $\underline{\underline{\tilde{F}}}$ in (7).

## 3. Experimental Results

To verify the proposed CI method, we conducted several experiments. Figure 2 shows the experimental setup, which consisted of two NEMA-17 stepper motors, an Adafruit Motor Shield V2, an Arduino Uno to control the stepper motors, a Texas Instruments FDC2214 capacitive sensing data acquisition board, a single-ended capacitive sensor, a differential capacitive sensor, a PVC pipe, wooden objects hidden inside the pipe, a PC, and a power supply. An aluminum-covered box was used to shield the sensors and the data acquisition board from the electromagnetic interferences while performing the data acquisitions.

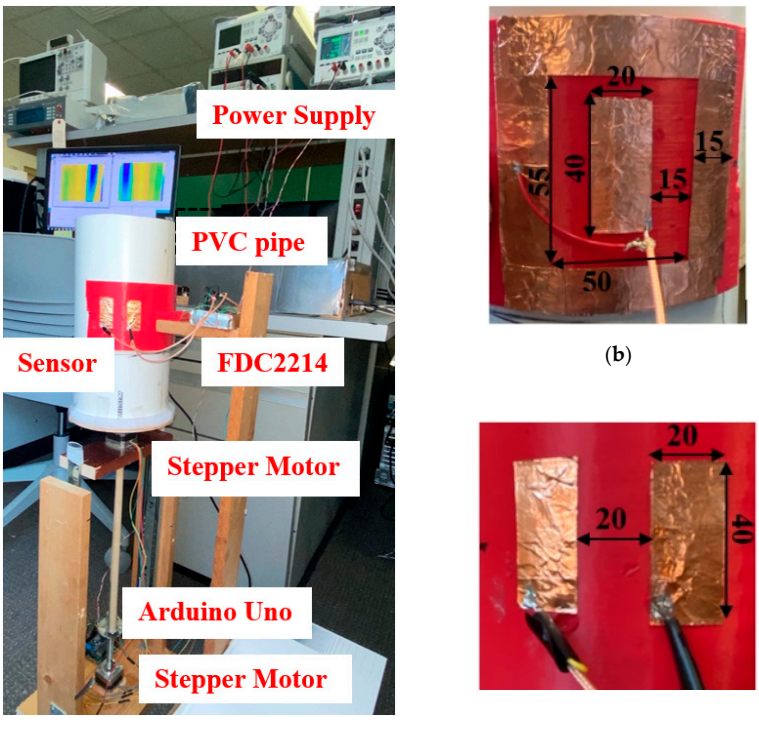


(**a**) (**b**) (**c**)

**Figure 2.** (**a**) Illustration of the cylindrical CI system with (**b**) single-ended sensor configuration and (**c**) differential sensor configuration. All dimensions are in mm.

For the experiments, we constructed two sensor configurations: a single-ended configuration and a differential configuration, as shown in Figure 2b,c, respectively. Differential configuration allowed the capacitive sensor to have higher sensitivity at close proximity while the single-ended configuration allowed the sensors to have a higher sensing range. The sensors were operated with the FDC2214 evaluation board manufactured

by Texas Instruments. This board was chosen as it is a multi-channel, high resolution (28-bit) capacitance-to-digital converter, is noise- and EMI-resistant, and can perform at high speed. It was used for detecting the changes of capacitance in the sensors via tracking the resonant frequency of an LC tank oscillator and communicating the changes in the responses with the Arduino Uno microcontroller through I2C communication. Two of the channels, CH2 and CH3, from FDC2214 were used to acquire the data from the customized capacitive sensors.

### *3.1. Configuration of the FDC2214 Module*

The data acquisition module, FDC2214, has a built-in LC tank for which, in this study, the changes in the capacitance could be observed as shifts in the resonant frequency. Typically, there was an 18 µH shielded SMD inductor in parallel with the capacitor, which resulted in oscillation. The FDC, which is a capacitance-to-digital converter, measured the oscillation frequency of the LC tank resonator and output a digital value that was proportional to the frequency that could be converted to an equivalent capacitance. This board supports two sensor configurations. In the single-ended configuration, a conductive plate is connected to one of the CHx pins, IN0A or IN0B, while in the differential configuration, two conductive plates are connected to two of the CHx pins. The FDC2214 data acquisition board uses differential configuration by default. To configure the single-ended sensors, we altered the FDC2214 module according to the datasheet provided by the manufacturer [27].

The FDC board has a maximum internal reference frequency $F_{REFx}$ of 55 MHz for multi-channel configuration. To utilize the multi-channel configuration of FDC2214, MUX_CONFIG with the address 0x1B was set to binary 1 for continuous conversion on multiple channels with 10 MHz of external oscillation. The $F_{INx}$ clock was derived from the sensor frequency for channel $x$. The reference frequency for Channel 0 ($CH_0$) to channel 3 ($CH_2$) was set by the $CH_x$_$F_{REFx}$_DIVIDER bit of the register $0 \times 14$ to $0 \times 17$. $F_{REFx}$ and $F_{INx}$ needed to meet the requirement of maximum reference frequency of 55 MHz and $F_{INx}$ ranges < 55/4 MHz = 13.75 MHz according to the datasheet (Texas Instrument 2020). The $CH_x$_$F_{IN}$_SEL domain of the register $0 \times 16$ for $CH_2$ was set to binary 10 for bit 13:14 and divider of 2 for $CH_2$_$F_{REF}$_DIVIDER to configure single-ended sensors [27]. The comprehensive value of the register $0 \times 16$ was $0 \times 2002$ (b001′0000′0000′0010) to set $CH_2$ as single-ended.

### *3.2. Data Acquisition and Imaged Objects*

The cylindrical positioning system allowed for scanning of the sensors over a two dimensional (2D) cylindrical aperture with 360 degrees of coverage and 120 mm of height. This was implemented by two stepper motors. The number of collected samples along the azimuthal and longitudinal directions were $N_\phi = 50$ and $N_z = 23$, respectively. A PVC pipe with a diameter of 152.4 mm (6 inches) and thickness of 7 mm was used for the imaging experiments. The imaged objects inside the PVC pipe were wooden pieces with dimensions of 50 mm × 44 mm × 20 mm. The goal was to image these objects at arbitrary positions along the azimuthal and longitudinal directions at two radial positions ($N_r$ = 2) of $r_1$ = 65 mm and $r_2$ = 45 mm. The two radial positions of $r_1$ and $r_2$ are referred to as shallow and deep radial depths, respectively. In the following, we describe three experiments along with the imaging results.

### *3.3. Imaging Results*

Multiple experiments were conducted to demonstrate the performance of the proposed CI technique. The wooden pieces were attached to the inner wall of the pipe. To obtain the PSF for the shallow depth ($r_1$ = 65 mm), namely $E_{i,1}^{CO}(\phi_k, z_l)$, one wooden piece was attached directly to the pipe's wall and the responses were collected over the cylindrical aperture. To obtain the PSF corresponding to the deep depth ($r_2$ = 45 mm), namely $E_{i,2}^{CO}(\phi_k, z_l)$, a piece of sponge was placed between a wooden piece and the pipe's wall. Sponge was selected due to the minimal effect on the responses of the sensors.

For a quantitative assessment of the reconstructed images, the structural similarity (SSIM) index [28] was computed for each image. SSIM is composed of three terms, the luminance term, the contrast term, and the structural term, as detailed in [28]. Here, the SSIM parameter was computed for each reconstructed image while we took the true object's image as the reference. To clarify further, in the reference image, pixels overlapping the objects had a value of 1 and other pixels had a value of 0. Thus, higher values of SSIM for an image indicated more similarity to the true image.

In the first test scenario, two wooden objects were placed only at shallow depth (directly attached to the inner pipe's wall) at $(r, \phi, z)$ coordinates of (65 mm, 0, 0) and (65 mm, 180°, 0). Figure 3 shows the reconstructed images when using the proposed CI technique described in Section 2 and using the data from both single-ended and differential sensors. It can be observed that the objects could be detected well in the images with brighter spots. In the second test, two wooden objects were placed only at deep depth (having sponge between the objects and the inner pipe's wall) at $(r, \phi, z)$ coordinates of (45 mm, 0, 0) and (45 mm, 180°, 0). Figure 4 shows the reconstructed images. The two objects could be detected well in their true positions in this scenario as well. In the third test, two wooden objects were placed at both the shallow and deep depths at coordinates of (65 mm, 0, 0) and (45 mm, 0, 0). Together, they represented a large object causing more clogging of the pipe. Figure 5 shows the reconstructed images for this scenario. The two objects could be detected well in their true positions in both the shallow and depth images.

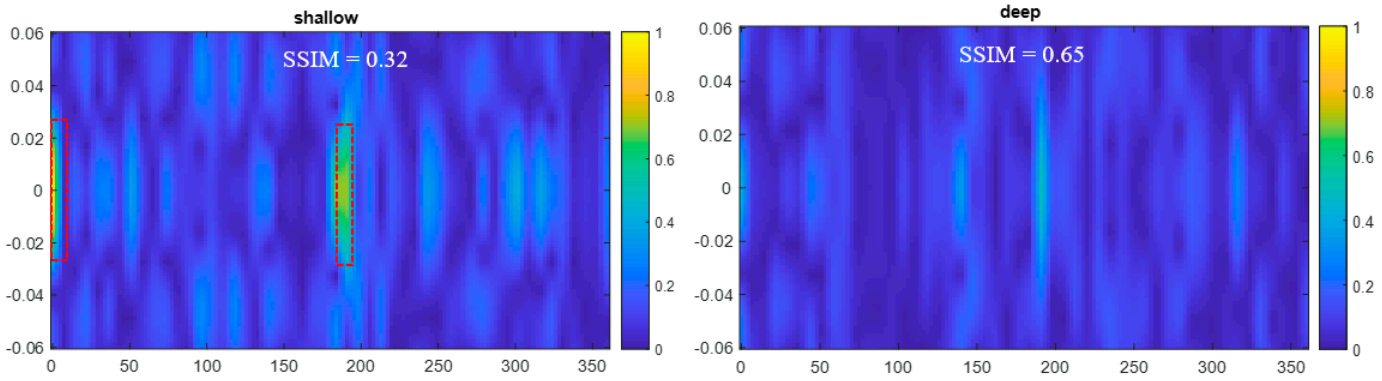


**Figure 3.** Reconstructed images when there were two objects at the shallow depth ($r_1$) at ($r$, $\Phi$, $z$) of (65 mm, 0, 0) and (65 mm,180°, 0). Dotted red lines show the true positions of the objects. Horizontal axis: $\Phi$ (degrees); vertical axis: $z$ (m).

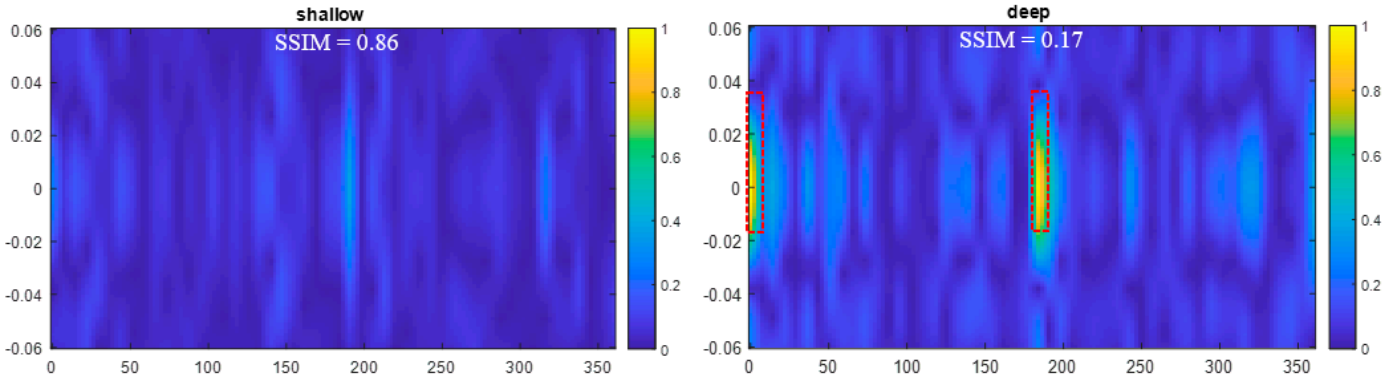


**Figure 4.** Reconstructed images when there were two objects at the deep depth ($r_2$) at ($r$, $\Phi$, $z$) of (45 mm, 0, 0) and (45 mm, 180°, 0). Dotted red lines show the true positions of the objects. Horizontal axis: $\Phi$ (degrees); vertical axis: $z$ (m).

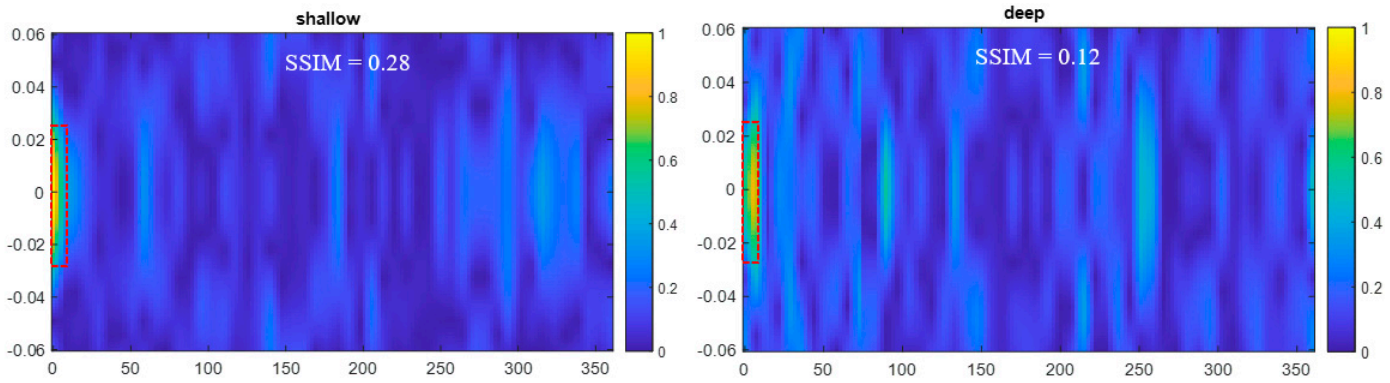


**Figure 5.** Reconstructed images when there were two objects at both the shallow and deep depths ($r_1$ and $r_2$) at ($r$, $\Phi$, $z$) of (65 mm, 0, 0) and (45 mm, 0, 0). Dotted red lines show the true positions of the objects. Horizontal axis: $\Phi$ (degrees); vertical axis: $z$ (m).

Overall, it was observed that the proposed CI technique provided qualitative images of the objects inside the pipes at various depths. In almost all the images, there were some artifacts, particularly in the images that contained the objects. However, the levels of the artifacts were much smaller than the levels of the true objects' images. Thus, the objects could be unambiguously detected in the reconstructed images.

To improve the resolution of the proposed CI technique, smaller conductor plates can be employed for the capacitive sensors. However, smaller plates should be compensated by the increase in the derived currents to the sensor plates to maintain sufficient strength of the inspecting fields which, in turn, would lead to a satisfactory range of inspection.

This nonintrusive technique can be used for security screening, inspection of clogging inside composite pipes, and nondestructive testing of flaws in composite pipes. Besides, this technique can be extended to rectangular imaging setups for nondestructive testing of multilayer dielectric structures, biomedical imaging, wall imaging, and underground imaging.

## 4. Discussion and Conclusions

In this paper, we proposed a CI technique for the imaging of dielectric or metallic objects hidden inside cylindrical media. We demonstrated that by using two capacitor sensor configurations (single-ended and differential), imaging of the objects at two depths from the measurement aperture is feasible. Larger numbers of sensors, with various sizes, shapes (square, rectangular, triangular, circular, elliptical, etc.), and configurations, can be employed for the imaging of objects over a larger number of radial depths. The sensors need to be optimized in terms of their sensitivity and range of sensing. Besides, their field distributions need to be sufficiently different so that their recorded responses add additional information to the systems of equations at each spatial frequency pair $\boldsymbol{\kappa} = (k_\phi, k_z)$ in (2).

The proposed CI technique provides qualitative images due to the approximations involved such as the linearity of the imaging system. The linearity assumption allows for the use of convolution theory which, in turn, leads to a fast and computationally efficient solution compared to the optimization-based techniques. Besides, breaking the original large system of equations in the spatial domain into the solution of many small systems of equations in the spatial frequency domain allows for more efficient and possibly parallel solutions, which can further expedite the image reconstruction process. This is important for real-time imaging applications. It is worth noting that linear models have been extensively employed in imaging applications based on the use of electromagnetic waves (e.g., see [29–32]). A prominent example of that is in the millimeter wave security screening of the passengers in airports [33], which, despite the linear approximations, provides high quality images. The methods based on the linearity assumptions, however, suffer image quality degradations for larger or higher contrast objects [34,35].

We believe one of the major reasons for having some artifacts in our experimental results (images) in the previous section is that the gap between the sensor holder and the pipe varied slightly during the scanning of the pipe along the azimuthal direction. This caused spurious variations in the responses, which in turn, produced undesired artifacts in the images. In general, to improve the quality of the images, we intend to take the following major steps in the future: (1) designing the shapes and dimensions of the sensors using numerical solvers for better sensitivity and larger difference between the spatial field distributions of the sensors (which adds more diversity of the collected data); (2) re-designing and re-building the scanning setup to minimize the variation of the gap between the sensors and the imaged pipe; and (3) adding more sensors with diverse spatial field distributions that allow for the collection of more information.

The use of readily available materials such as wood and PVC pipe helped to conduct fast and low-cost proof-of-concept experiments. The utilized setup can also be relevant to the following applications: the inspection of clogging of pipes, and security screening for imaging of hidden objects. According to our experiments, the responses received by smaller wooden pieces were weaker, leading to more erroneous images. Thus, the dimensions of the imaged wooden pieces in this paper can be considered as the minimum sizes for which reliable and high-quality images can be reconstructed. Besides, as per our preliminary observations, in applications where the imaged objects were highly conductive (such as metallic objects), the measured responses were stronger, leading to better image qualities. However, those objects could be also measured by inductive sensors rather than capacitive sensors to avoid interferences from nonconductive background objects in the scanning setup.

**Author Contributions:** Conceptualization, R.K.A.; methodology, R.K.A. and M.R.; software, N.R., Y.G. and M.G.; validation, N.R., Y.G., M.G. and M.R.; formal analysis, N.R., Y.G. and M.R.; investigation, all authors; resources, R.K.A. and M.R.; data curation, R.K.A. and M.R.; writing—original draft preparation, N.R. and M.R.; writing—review and editing, R.K.A. and M.R.; visualization, all authors; supervision, R.K.A. and M.R.; project administration, R.K.A. and M.R.; funding acquisition, R.K.A. All authors have read and agreed to the published version of the manuscript.

**Funding:** This project has been supported by the US National Science Foundation (NSF), award No. 1920098, and the New York Institute of Technology's Institutional Support for Research and Creativity (ISRC) Grant.

**Conflicts of Interest:** The authors declare no conflict of interest.

## References

1. Liu, Z.; Huan, L. Experimenting capacitive sensing technique for structural integrity assessment. In Proceedings of the IEEE International Conference on Industrial Technology (ICIT), Toronto, ON, Canada, 22–25 March 2017.
2. Schmidt, S.; Schusler, M.; Damm, C.; Schuster, C.; Jakoby, R. Concept and design of a 40 GHz differential sensor for the analysis of biomedical substances. In Proceedings of the 2016 IEEE Topical Conference on Biomedical Wireless Technologies, Networks, and Sensing Systems (Bio-WireleSS) , Austin, TX, USA, 24–27 January 2016.
3. Ambika, M.; Selva, K.S. Modeling and calibration of electrical capacitance tomography sensor for medical imaging. *Biomed. Pharmacol. J.* **2018**, *11*, 1471–1477. [CrossRef]
4. Yang, W. Key issues in designing capacitance tomography sensors. *IEEE Conf. Sens.* **2006**, 497–505. [CrossRef]
5. Genest, M.; Krys, D.; Mandache, C. Capacitive sensing for the detection of tile misalignment in ceramic armor arrays. *NDT E Int.* **2020**, *112*, 102261. [CrossRef]
6. Yin, X.; Hutchins, D. Non-destructive evaluation of composite materials using a capacitive imaging technique. *Compos. Part B Eng.* **2012**, *43*, 1282–1292. [CrossRef]
7. Yin, X.; Diamond, G.G.; Hutchins, D.A. Further investigations into capacitive imaging for NDE. *Insight-Non-Destr. Test. Cond. Monit.* **2009**, *51*, 484–490. [CrossRef]
8. Diamond, G.; Hutchins, D.A. A new capacitive imaging technique for NDT. In Proceedings of the European Conference on NDT, Berlin, Germany, 25–29 September 2006.
9. Dérobert, X.; Iaquinta, J.; Klysz, G.; Balayssac, J. Use of capacitive and GPR techniques for the non-destructive evaluation of cov-er concrete. *NDT E Int.* **2008**, *41*, 44–52. [CrossRef]
10. Li, X.; Larson, S.; Zyuzin, A.; Mamishev, A. Design principles for multichannel fringing electric field sensors. *IEEE Sens. J.* **2006**, *6*, 434–440. [CrossRef]

11. Jaworski, A.J.; Bolton, G.T. The design of an electrical capacitance tomography sensor for use with media of high dielectric per-mittivity. *Meas. Sci. Technol.* **2000**, *11*, 743–757. [CrossRef]
12. Elkow, K.; Rezkallah, K. Void fraction measurements in gas-liquid flows under 1-g and μ-g conditions using capacitance sensors. *Int. J. Multiph. Flow* **1997**, *23*, 815–829. [CrossRef]
13. Jin, B.; Zhang, Z.; Zhang, H. Structure design and performance analysis of a coaxial cylindrical capacitive sensor for liquid-level measurement. *Sens. Actuators A Phys.* **2015**, *223*, 84–90. [CrossRef]
14. Ye, Y.; Deng, J.; Shen, S.; Hou, Z.; Liu, Y. A novel method for proximity detection of moving targets using a large-scale planar ca-pacitive sensor system. *Sensors* **2016**, *16*, 699. [CrossRef]
15. Xia, F.; Campi, F.; Bahreyni, B. Tri-Mode Capacitive Proximity Detection Towards Improved Safety in Industrial Robotics. *IEEE Sens. J.* **2018**, *18*, 5058–5066. [CrossRef]
16. Wang, K.; Yin, X.; Li, C.; Li, W.; Chen, G. Capacitive Imaging Technique for the Inspection of Composite Sucker Rod. *Chin. J. Mech. Eng.* **2019**, *32*, 105. [CrossRef]
17. Texas Instruments. *FDC1004: Basics of Capacitive Sensing and Applications*; Texas Instruments: Dallas, TX, USA, 2021; Available online: https://www.ti.com/lit/an/snoa927a/snoa927a.pdf (accessed on 2 December 2021).
18. Hu, X.; Yang, W. Planar capacitive sensors–designs and applications. *Sens. Rev.* **2010**, *30*, 24–39. [CrossRef]
19. Yin, X.; Hutchins, D.A.; Chen, G.; Li, W. Preliminary studies on the design principles of capacitive imaging probes for non-destructive evaluation. *Int. J. Appl. Electromagn. Mech.* **2013**, *42*, 447–470. [CrossRef]
20. Kirby, T.W. Capacitive Sensor Technology for Polyethylene Pipe Fault Detection. Master's Thesis, West Virginia University, Morgantown, WV, USA, 2019. [CrossRef]
21. Pascual-Marqui, R.D. 3D distributed, linear imaging methods of electric neuronal activity. Part 1: Exact, zero error localization Math. *arXiv* **2007**, arXiv:0710.3341.
22. Pascual-Marqui, R. Review of Methods for Solving the EEG Inverse Problem. *Int. J. Biomagn.* **1999**, *1*, 75–86.
23. Oppenheim, A.V.; Schafer, R.W.; Buck, J.R. *Discrete-Time Signal Processing*, 2nd ed.; Prentice Hall: Upper Saddle River, NJ, USA, 1999.
24. Ravan, M.; Amineh, R.K.; Hussein, A.; Simanov, O.; Agarwal, A. Electromagnetic Induction Imaging of Metallic Objects at Multiple Depths. *IEEE Magn. Lett.* **2020**, *11*, 2100405. [CrossRef]
25. Wu, H.; Ravan, M.; Sharma, R.; Patel, J.; Amineh, R.K. Microwave Holographic Imaging of Nonmetallic Concentric Pipes. *IEEE Trans. Instrum. Meas.* **2020**, *69*, 7594–7605. [CrossRef]
26. Wu, H.; Ravan, M.; Amineh, R.K. Holographic Near-Field Microwave Imaging With Antenna Arrays in a Cylindrical Setup. *IEEE Trans. Microw. Theory Tech.* **2021**, *69*, 418–430. [CrossRef]
27. Texas Instruments. *FDC2x1x EMI-Resistant 28-Bit,12-Bit Capacitance-to-Digital Converter for Proximity and Level Sensing Applications*; Texas Instruments: Dallas, TX, USA, 2020; Available online: https://www.ti.com/lit/ds/symlink/fdc2214.pdf (accessed on 2 December 2021).
28. Zhou, W.; Bovik, A.C.; Sheikh, H.R.; Simoncelli, E.P. Image quality assessment: From error visibility to structural similarity. *IEEE Trans. Image Process.* **2004**, *13*, 600–612.
29. Karbeyaz, B.U.; Gencer, N.G. Electrical conductivity imaging via contactless measurements: An experimental study. *IEEE Trans. Med. Imag.* **2003**, *22*, 627–635. [CrossRef]
30. Igney, C.H.; Watson, S.; Williams, R.J.; Griffiths, H.; Dössel, O. Design and performance of a planar-array MIT system with normal sensor alignment. *Physiol. Meas.* **2005**, *26*, S263–S278. [CrossRef] [PubMed]
31. Ma, L.; Wei, H.-Y.; Soleimani, M. Planar magnetic induction tomography for 3D near subsurface imaging. *Prog. Electromagn. Res.* **2013**, *138*, 65–82. [CrossRef]
32. Watson, S.; Williams, R.J.; Gough, W.; Griffiths, H. A magnetic induction tomography system for samples with conductivities below 10 S m−1. *Meas. Sci. Technol.* **2008**, *19*, 045501. [CrossRef]
33. Sheen, D.; McMakin, D.; Hall, T. Three-dimensional millimeter-wave imaging for concealed weapon detection. *IEEE Trans. Microw. Theory Tech.* **2001**, *49*, 1581–1592. [CrossRef]
34. Amineh, R.K.; Ravan, M.; Khalatpour, A.; Nikolova, N.K. Three-dimensional near-field microwave holography using reflect-ed and transmitted signals. *IEEE Trans. Antennas Propag.* **2011**, *59*, 4777–4789. [CrossRef]
35. Amineh, R.K.; Nikolova, N.K.; Ravan, M. *Real-Time Three Dimensional Imaging of Dielectric Bodies Using Micro-Wave/Millimeter Wave Holography*; Wiley: Hoboken, NJ, USA, 2019.